

Technical Note: A new discrete ordinate first-order rotational Raman scattering radiative transfer model – implementation and first results

A. Kylling¹, B. Mayer², and M. Blumthaler³

¹NILU-Norwegian Institute for Air Research, Kjeller, Norway

²Meteorological Institute, Ludwig-Maximilians-University, Munich, Germany

³Division for Biomedical Physics, Innsbruck Medical University, Innsbruck, Austria

Received: 10 August 2010 – Published in Atmos. Chem. Phys. Discuss.: 1 October 2010

Revised: 23 September 2011 – Accepted: 10 October 2011 – Published: 21 October 2011

Abstract. Rotational Raman scattering in the Earth's atmosphere explains the filling-in of Fraunhofer lines in the solar spectrum. A new model including first-order rotational Raman scattering has been developed, based on a reimplementation of the versatile discrete ordinate radiative transfer (DISORT) solver in the C computer language. The solver is fully integrated in the freely available libRadtran radiative transfer package. A detailed description is given of the model including the spectral resolution and a spectral interpolation scheme that considerably speeds up the calculations. The model is used to demonstrate the effect of clouds on top and bottom of the atmosphere filling-in factors and differential optical depths. Cloud effects on vertical profiles of the filling-in factor are also presented. The spectral behaviour of the model is compared against measurements under thunderstorm and aerosol loaded conditions.

1 Introduction

Rotational Raman scattering (RRS) explains the filling-in of Fraunhofer lines in solar spectra measured both from the Earth's surface and onboard satellites (Kattawar et al., 1981). The filling-in is also called the “Ring effect” after Grainger and Ring (1962). RRS is of importance because it affects the retrieval accuracy of both column amounts and profiles of trace gases (e.g. Solomon et al., 1987; Hoogen et al., 1999; Hasekamp and Landgraf, 2001; Vountas et al., 1998). Furthermore, the RRS signal may be used to estimate cloud pres-

sure information from satellite measurements (Joiner and Bhartia, 1995; Joiner et al., 2004, 2010; Joiner and Vasilkov, 2006, e.g.) and aerosol properties from both surface and satellite observations (Wagner et al., 2009b, 2010). Radiative transfer models that include RRS are thus needed for the interpretation and analysis of radiation measurements of the Earth's atmosphere.

Many numerical models exist for the treatment of elastic multiple scattering of photons in the Earth's atmosphere. The inclusion of inelastic scattering is more demanding and typically RRS is treated as a perturbation with only first-order RRS being accounted for. Several authors have developed radiative transfer models that account for RRS, including Joiner et al. (1995); Vountas et al. (1998); Landgraf et al. (2004); van Deelen et al. (2005); Spurr et al. (2008); Wagner et al. (2009a).

The model of Joiner et al. (1995) is a vector successive order of scattering code including first-order RRS. Vountas et al. (1998) described a first-order RRS finite difference model that treated clouds and aerosols explicitly. This model was used by de Beek et al. (2001) to study the effect of RRS on both ground-based and satellite measurements. Spurr et al. (2008) described a discrete ordinates method model for first-order RRS and presented model simulations of filling-in factors due to RRS in cloudy situations. Results for both satellite geometries and vertical profiles of filling-in factors were shown. Wagner et al. (2009a) presented the first 3-D Monte Carlo simulations of first-order RRS in the presence of horizontally inhomogeneous (cubical) clouds. This model has been used to determine aerosol properties from both surface multi-axis differential optical absorption spectroscopy (MAX-DOAS) observations of the Ring effect (Wagner et al.,



Correspondence to: A. Kylling
(arve.kylling@nilu.no)

2009b) and satellite observations of the Ring effect (Wagner et al., 2010).

All the above codes except the code of Joiner et al. (1995), are scalar, that is, they do not include polarization. Landgraf et al. (2004) presented a first-order RRS vector radiative transfer model based on the Gauss-Seidel approximation. They found that the inclusion of polarization on Raman scattering is of minor importance for most applications. van Deelen et al. (2005) developed a doubling-adding code including multiple elastic scattering and multiple inelastic RRS. They found that multiple RRS contributes about 0.2–0.6 % to the radiance (including all orders of RRS) for the cases they investigated.

In this paper a new discrete ordinates radiative transfer model including first-order RRS is presented. The model is based on a recent re-write (Buras et al., 2011) of the discrete-ordinate-method radiative transfer algorithm (DISORT, Stamnes et al., 1988). The main difference between this work and the discrete-ordinate model of Spurr et al. (2008) is in the solution of the particular integrals for the Raman scattering gain and loss terms. Calculations including RRS are computer intensive due to the large number of Raman lines involved. A simple method for increasing the computing speed with minimal loss of accuracy is also presented.

The paper is organized as follows: First a detailed description is given of the radiative transfer model. Secondly, examples are given of RRS effects in cloudy atmospheres. This is followed by a comparison of model results and measurements for a thunderstorm situation and an aerosol case.

2 Inclusion of RRS in the libRadtran radiative transfer model

The radiative transfer equation including first-order RRS, has been derived by for example Vountas et al. (1998) and Landgraf et al. (2004). For radiation, $I(r, \Omega, \lambda)$, at wavelength λ , location r , and travelling in the direction Ω , the radiative transfer equation including RRS may be written as (Vountas et al., 1998, Eq. 10)

$$\mathcal{R}I(r, \Omega, \lambda) = \varepsilon_{\text{RRS}}(r, \Omega, \lambda), \quad (1)$$

where $\{\Omega\} = \{\mu, \phi\}$, μ is the cosine of the polar angle and ϕ is the azimuth angle. The integro-differential operator \mathcal{R} in a one dimensional atmosphere is

$$\mathcal{R} = \mu \frac{d}{dr} + \beta^{\text{ext}}(r, \lambda) - \frac{\beta^{\text{sca}}(r, \lambda)}{4\pi} \int d\Omega' P(r, \Omega, \Omega', \lambda). \quad (2)$$

Here $P(r, \Omega, \Omega', \lambda)$ is the phase function, $\beta^{\text{ext}} = \beta^{\text{abs}} + \beta^{\text{sca}}$, $\beta^{\text{abs}}(r, \lambda) = \sum_i \beta_i^{\text{abs}}(r, \lambda)$, $\beta_i^{\text{abs}}(r, \lambda) = n_i(r) \sigma_i^{\text{abs}}(\lambda)$ and similarly for the scattering coefficient $\beta_i^{\text{sca}}(r, \lambda)$ (Stamnes, 1986). The vertical profile of species i is denoted by $n_i(r)$, and $\sigma_i(\lambda)$ is the corresponding absorption or scattering cross section. The summation over i for β^{sca} includes Rayleigh scattering,

and scattering of aerosols and clouds. The Rayleigh scattering consists of the central Cabannes line and rotational Raman scattering (Young, 1981). The absorption coefficient includes absorption by clouds, aerosols and various molecular species. Finally

$$\begin{aligned} \varepsilon_{\text{RRS}}(r, \Omega, \lambda) = & \sum_{s=1}^N \frac{\beta_{\text{RRS}}(r, \lambda_s, \lambda)}{4\pi} \int d\Omega' I(r, \Omega', \lambda_s) P_{\text{RRS}}(\Omega, \Omega', \lambda_s) \\ & - \sum_{s=1}^N \frac{\beta_{\text{RRS}}(r, \lambda, \lambda_s)}{4\pi} \int d\Omega' I(r, \Omega', \lambda) P_{\text{RRS}}(\Omega, \Omega', \lambda), \end{aligned} \quad (3)$$

where β_{RRS} is the RRS coefficient and the Raman phase function $P_{\text{RRS}}(\Theta) = 3/40(13 + \cos^2 \Theta)$ with $\cos \Theta = -\mu\mu' + \sqrt{1-\mu'^2}\sqrt{1-\mu^2}\cos(\Phi - \Phi')$. The first term on the right hand side of Eq. (3) represents photons that are Raman scattered from other wavelengths λ_s into the wavelength λ of interest. Similarly, the second term represents photons that are Raman scattered out of the wavelength λ and into the Raman lines λ_s . It is noted that the last term on the right-hand side of Eq. (3) is not a real physical source of radiation. Rather, it is due to the use of the Rayleigh scattering cross section instead of the Cabannes cross section in β^{sca} (van Deelen et al., 2005; Spurr et al., 2008). Neglecting Raman scattering and setting $\varepsilon_{\text{RRS}}(r, \Omega, \lambda) = 0$, gives the standard 1-D radiative transfer equation for elastic scattering, see e.g. Chandrasekhar (1960). From the radiance, $I(\tau, \mu, \Phi)$, the diffuse up- (E^+) and down-welling (E^-) irradiances may be calculated through:

$$E^\pm(\tau) = \int_0^{2\pi} d\Phi \int_0^1 d\mu I(\tau, \pm\mu, \Phi). \quad (4)$$

The solution of Eq. (1) starts with the splitting of the global (direct plus diffuse) radiation field in a direct and a diffuse component. By expanding the radiance in a Fourier cosine series, $I(\tau, \pm\mu, \Phi) = \sum_{m=0}^{2N-1} I_m(\tau, \pm\mu) \cos m(\Phi_0 - \Phi)$ where Φ_0 is the azimuth incidence angle of the direct solar beam, writing the phase function in terms of Legendre polynomials, applying the addition theorem for spherical harmonics and replacing the integral over μ in Eq. (1) with a sum using double Gaussian quadrature, the discrete ordinate version of Eq. (1) is obtained (Chandrasekhar, 1960; Stamnes et al., 1988; Spurr et al., 2008):

$$\begin{aligned} \mu_i \frac{dI^m(\tau_\lambda, \mu_i)}{d\tau_\lambda} &= I^m(\tau_\lambda, \mu_i) \\ & - \frac{\omega^E(\tau, \lambda)}{2} \sum_{\substack{j=-N \\ j \neq 0}}^j c_j \Pi_d^E(\tau_\lambda, \mu_i, \mu_j) I^m(\tau_\lambda, \mu_j) \\ & - \frac{\omega^E(\tau, \lambda) I_\lambda^0}{4\pi} (2 - \delta_{0,m}) \Pi_b^E(\tau_\lambda, \mu_i, \mu_0) e^{-T(\tau_\lambda)} \\ & - Q^m(\tau_\lambda, \mu_i), \end{aligned} \quad (5)$$

$$\begin{aligned}
Q^m(\tau_\lambda, \mu_i) = & \\
& + \sum_{s=1}^{NS} \frac{\omega^R(\tau, \lambda_s, \lambda)}{2} \sum_{\substack{j=N \\ j \neq 0}}^{j=N} c_j \Pi_d^R(\tau_{\lambda_s}, \mu_i, \mu_j) I^{E,m}(\tau_{\lambda_s}, \mu_j) \\
& + \sum_{s=1}^{NS} \frac{\omega^R(\tau, \lambda_s, \lambda) I_{\lambda_s}^0}{4\pi} (2 - \delta_{0,m}) \Pi_b^R(\tau_{\lambda_s}, \mu_i, \mu_0) e^{-T(\tau_{\lambda_s})} \\
& - \frac{\omega^{RL}(\tau, \lambda)}{2} \sum_{\substack{j=N \\ j \neq 0}}^{j=N} c_j \Pi_d^R(\tau_\lambda, \mu_i, \mu_j) I^{E,m}(\tau_\lambda, \mu_j) \\
& - \frac{\omega^{RL}(\tau, \lambda) I_\lambda^0}{4\pi} (2 - \delta_{0,m}) \Pi_b^R(\tau_\lambda, \mu_i, \mu_0) e^{-T(\tau_\lambda)}, \quad (6) \\
& (i = \pm 1, \dots, \pm N; m = 0, 1, 2, \dots, 2N-1),
\end{aligned}$$

The three different single scattering albedos for the elastic (E), Raman gain (R) and Raman loss (RL) scattering terms are calculated according to Stamnes (1986); Spurr et al. (2008) as:

$$\omega^E(\tau, \lambda) = \frac{\beta^{\text{sca}}(\tau, \lambda)}{\beta^{\text{ext}}(\tau, \lambda)} \quad (7)$$

$$\omega^R(\tau, \lambda_s, \lambda) = \frac{\rho_{\text{air}}(\tau) (\zeta_{O_2} \sigma_{O_2}^{\text{RRS}}(\lambda_s, \lambda) + \zeta_{N_2} \sigma_{N_2}^{\text{RRS}}(\lambda_s, \lambda))}{\beta^{\text{ext}}(\tau, \lambda_s)} \quad (8)$$

$$\omega^{RL}(\tau, \lambda) = \frac{\rho_{\text{air}}(\tau) \left(\zeta_{O_2} \sum_{s=1}^{NS_{O_2}} \sigma_{O_2}^{\text{RRS}}(\lambda, \lambda_s) + \zeta_{N_2} \sum_{s=1}^{NS_{N_2}} \sigma_{N_2}^{\text{RRS}}(\lambda, \lambda_s) \right)}{\beta^{\text{ext}}(\tau, \lambda)} \quad (9)$$

where $\rho_{\text{air}}(\tau)$ is the density of air and the relative abundances of O_2 and N_2 are set to $\zeta_{O_2} = 0.2095$ and $\zeta_{N_2} = 0.7905$. A total of $NS = 233$ Raman lines, $NS_{O_2} = 185$ for O_2 and $NS_{N_2} = 48$ for N_2 , are considered following Chance and Spurr (1997) and de Haan (2003). The elastic single scattering albedo ω_λ^E is the same as used in the elastic calculation and includes the Rayleigh cross section. The RRS cross section is denoted by σ^{RRS} and is given by (see Chance and Spurr (1997); Spurr et al. (2008) and references therein)

$$\sigma^{\text{RRS}}(\lambda, \lambda^s) = \frac{256\pi^5}{27\lambda_s^4} f_N(T) \gamma^2(\lambda) C_{J \rightarrow J'}, \quad (10)$$

where $f_N(T)$ is the temperature dependent state fractional population, $C_{J \rightarrow J'}$ is the Placzek-Teller coefficients and $\gamma(\lambda)$ is the anisotropy factor.

The phase function is expanded in associated Legendre polynomials $\Lambda_l^m(\mu)$ as

$$\Pi_b^{x,m}(\tau, \mu, \mu_0) = \sum_{l=m}^{2M-1} (2l+1) g_l^x(\tau) (-1)^{l+m} \Lambda_l^m(\mu) \Lambda_l^m(\mu_0) \quad (11)$$

$$\Pi_d^{x,m}(\tau, \mu, \mu') = \sum_{l=m}^{2M-1} (2l+1) g_l^x(\tau) \Lambda_l^m(\mu) \Lambda_l^m(\mu'), \quad (12)$$

where $x = E, \text{RRS}$. For the Raman phase function only terms with $m = 0, 1, 2$ contribute in the above sums. The phase function expansion coefficients are defined by

$$g_l^x(\tau) = \frac{1}{2} \int_{-1}^1 P_l^x(\cos \Theta) \Pi^x(\tau, \cos \Theta) d\cos \Theta \quad (13)$$

where $P_l(\cos \Theta)$ is the l th Legendre polynomial. For Rayleigh and Raman scattering $g_0 = 1$ and $g_1 = 0$, while $g_2^{\text{RRS}} = 1/20$ and $g_2^{\text{Ray}} = (1-\rho)/(2+\rho)$ where ρ is the depolarization ratio. For the Rayleigh and Raman scattering phase functions all higher terms are zero.

The solar beam transmission $T(\tau)$ is calculated in pseudo-spherical geometry to account for the sphericity of the Earth's atmosphere (Dahlback and Stamnes, 1991). The optical depth at wavelength s is denoted by τ_s .

In Eqs. (5)–(6) the number of quadrature points are $2N$ and μ_i and c_i are quadrature angles and weights respectively. If not otherwise noted, all calculations were performed with 16 streams, or $N = 8$. Strongly peaked phase functions are handled with an improved version of the Nakajima and Tanaka (1988) correction method (Buras et al., 2011).

Equation (5)–(6) are a system of $2N$ coupled differential equations for which analytic solutions do not exist due to the τ dependence of the phase function and the single scattering albedo. By the assumption that the atmosphere consists of L adjacent layers where the single scattering albedo and the phase function are assumed to be constant, analytic solutions may be obtained for each layer. The analytic solutions for each layer are coupled by requiring the intensity to be continuous across layer interfaces. General boundary conditions are applied including a bidirectional reflectance function at the bottom of the atmosphere, see Stamnes et al. (1988) for further details.

Only a small fraction ($\sim 4\%$) of the photons in the Earth's atmosphere are Raman scattered. Following Vountas et al. (1998), ε_{RRS} is treated as a perturbation and an iterative solution of Eq. (1) is sought. The zeroth order solution, $I^{(0)}(\tau, \Omega, \lambda) = I^E(\tau, \Omega, \lambda)$, is then the solution of Eq. (5) with $Q^m(\tau_\lambda, \mu_i) = 0$. It is solved with the discrete ordinate method of Stamnes et al. (1988) including pseudo-spherical geometry using an exponential-linear in optical depth approximation (Dahlback and Stamnes, 1991; Kylling and Stamnes, 1992). The first order solution, $I^{(1)}(\tau, \Omega, \lambda) = I^{(0)}(\tau, \Omega, \lambda) + \mathcal{R}^{-1} \varepsilon_{\text{RRS}}^{(0)}(\tau, \Omega, \lambda)$, is calculated in the next iteration using $I^{(0)}(\tau, \Omega, \lambda)$ to calculate $Q^m(\tau_\lambda, \mu_i)$.

As shown in Spurr et al. (2008, Eq. 26), all the terms on the right hand side of Eq. (6) have exponential in optical depth dependence. However, using an exponential substitution method for the RRS particular integral solution leads to degenerate linear algebra problems (see Spurr et al. (2008) for details). Spurr et al. (2008) overcame the degeneracy by adopting a Green's function solution without the need for any approximations. To avoid the degeneracy here, the source $Q^m(\tau_\lambda, \mu_i)$ in Eq. (6) is assumed to be constant over individual layers. Thus, the source is allowed to vary from layer to

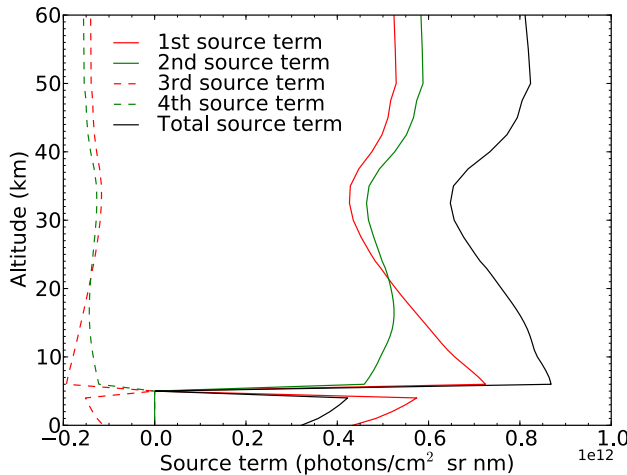


Fig. 1. The total RRS source term $Q^0(\tau_\lambda, \mu_i)$ in Eq. (6) (black line) and the individual terms on the right hand side of Eq. (6) in the order they occur. The source is shown for a quadrature angle $\mu_i = 0.02$. The shape of the full source and source terms are similar for the other quadrature angles. The wavelength is 393.37 nm, close to the center of the calcium K line. A water cloud of optical depth 10.0 is included between 5 and 6 km. The solar zenith angle is 33° and the surface albedo is 0.03.

layer, but has no dependence of optical depth within a layer. For a given layer the source is calculated as the mean value of Eq. (6) at the bottom and top of the layer. An example of the approximated total RRS source term $Q^m(\tau_\lambda, \mu_i)$ in Eq. (6), is shown in Fig. 1 together with the four individual source terms on the right hand side of Eq. (6).

A particular solution of the form

$$I^m(\tau, \mu_i) = Y^m(u_i) \quad (14)$$

is sought for each layer. The coefficients $Y^m(u_i)$ are found by solving linear algebraic equations (Stamnes and Swanson, 1981). The solution of Eq. (5) including the RRS source term $Q(\tau_\lambda, \mu_i)$ has been included in the new C-version of the DISORT Stamnes et al. (1988) algorithm (Buras et al., 2011). This algorithm has been adopted in the libRadtran radiative transfer package (Mayer and Kylling, 2005) to solve Eq. (1) for first-order RRS including absorption and multiple elastic scattering of molecules, aerosols and clouds.

2.1 Filling-in factor and other quantities

The filling-in factor FI is often used to describe the magnitude of RRS. It involves the ratio of modelled radiation quantities with and without RRS. Several definitions of the filling-in factor are used in the literature (Joiner and Bhartia, 1995; Spurr et al., 2008). Here, the definition of Spurr et al. (2008) is adopted,

$$\text{FI}(\lambda) = 100 \% \left(1 - \frac{E_{\text{elastic}}(\lambda)}{E_{\text{inelastic}}(\lambda)} \right), \quad (15)$$

where E_{elastic} and $E_{\text{inelastic}}$ are the calculated irradiances without and with RRS, respectively. A similar expression is used to calculate the filling-in factor from radiances $I(\tau, \mu)$. For vertical profiles the filling-in is calculated locally, that is, both E_{elastic} and $E_{\text{inelastic}}$ are calculated at the same altitude.

To compare model results with irradiance measurements the differential optical depth, DOD, was calculated,

$$\text{DOD}(\lambda) = \ln(E(\lambda)/E_{\text{ref}}(\lambda)) - P(\lambda). \quad (16)$$

Here, E^{ref} is the reference spectrum, E the spectrum of interest, and P a third degree polynomial that accounts for broadband features including Rayleigh scattering, aerosol absorption and scattering, and cloud scattering in the wavelength region under investigation.

The number of photons that are Raman scattered depends on both the concentration of the air molecules, that is, altitude, and the pathlength traversed by the photons. It is illustrative to look at the change in photon pathlength when for example clouds and aerosol are present in the atmosphere. An effective pathlength l_{eff} may be defined as (see Mayer et al. (1998) and references therein)

$$E_{\text{abs}} = E_{\text{no abs}} \exp(-\tau_{\text{abs}} l_{\text{eff}}/d) = E_{\text{no abs}} \exp(-\tau_{\text{abs}} \xi_{\text{eff}}). \quad (17)$$

Here, the macroscopic effective pathlength enhancement, $\xi_{\text{eff}} = l_{\text{eff}}/d$, where d is the geometrical height of the cloud or aerosol layer. Furthermore, E_{abs} is the radiation quantity of interest calculated with an additional absorber of small optical depth τ_{abs} while $E_{\text{no abs}}$ is the same quantity without the extra absorber.

2.2 Solar spectrum and spectral considerations

Calculations including RRS require an extra-terrestrial (ET) solar spectrum. Here the revised high-resolution Kurucz solar spectrum is adopted (Kurucz, 1992; Fontenla et al., 1999). The spectrum was obtained from the “Solar source function” of Clough et al. (2005). In the spectral region from 316.7 to 415 nm the absolute magnitude of the revised Kurucz spectrum exhibits absolute broad wavelength deviations compared with other established spectra (Gurlit et al., 2005). The Kurucz spectrum was therefore scaled to the Atlas 3 spectrum (Woods et al., 1996). For comparison with ground-based measurements the spectrum was resampled to air wavelengths using the refractive index for air from Lide (2009). Following Chance and Spurr (1997) the spectrum was resampled at even 0.01 nm increments using a triangular filter with full-width at half-maximum (FWHM) of 0.02 nm.

To calculate the radiation at wavelength λ , the elastically scattered radiation is needed at the wavelengths of the 233 Raman lines. The radiation field at these wavelengths may either be obtained by solving the zeroth order radiative transfer equation for each wavelength, or, to save computer time, by solving the radiative transfer equation at a coarser spectral resolution and interpolating the radiation field to the Raman

lines. Both approaches have been implemented. Comparisons of the two approaches in the Ca H and K lines region, with “coarse” resolution taken to be 0.01 nm, showed that the differences between them are negligible. The interpolation approach significantly reduces the computation time. The reduction depends on the application, but is on the order of 10–100.

The output from the present solution is provided at the same wavelength grid as the input ET-spectrum. Internally the zero order simulation is made at the resolution of the ET-spectrum and the results stored in memory. As the resolution of the ET-spectrum determines the resolution of the simulation, species with sharp spectral absorptions may easily be considered by simply using an ET-spectrum with a sufficiently high resolution to resolve the spectral absorption features.

As discussed by Spurr et al. (2008) one may either use a high-resolution ET spectrum as input and convolve the result with the instrument response function; or one may use an ET spectrum measured by the instrument to be simulated. Alternatively to the last approach one may convolve the high-resolution ET spectrum with the instrument response function prior to the simulation. This latter approach is attractive for ground-based instruments for which ET spectral measurements are not available. To investigate possible differences between the various approaches, the following simulations were carried out for the Bentham spectroradiometer in Garmisch-Partenkirchen with a slit function FWHM of 0.5 nm, (see Sect. 4.1 for further details), for the 390–400 nm interval which includes the strong calcium K and H lines:

1. Simulation with an ET-spectrum with 0.01 nm resolution. The spectrum was generated as described above. The simulated spectrum was convolved with the instrument response function.
2. The high-resolution ET spectrum from 1) was convolved with the instrument response function prior to the simulation. The simulation was carried out at 0.01 nm resolution.
3. The high-resolution ET spectrum was convolved with the instrument response function prior to the simulation. The simulation was made at 0.05 nm resolution.

For the simulations the solar zenith angle was 75°, the surface albedo was set to zero and neither clouds nor aerosol were included. Filling-in factors were determined from downwelling BOA irradiances calculated with and without RRS. In Fig. 2 the filling-in factors are shown for the various spectral approaches. The high-resolution result without any instrument response function is shown by the green line. The other results involve the various approaches of treating the instrument spectral response function and are indistinguishable. Hence, all further simulations are performed with an ET-spectrum at 0.05 nm resolution convolved with the appropriate instrument response function unless otherwise noted.

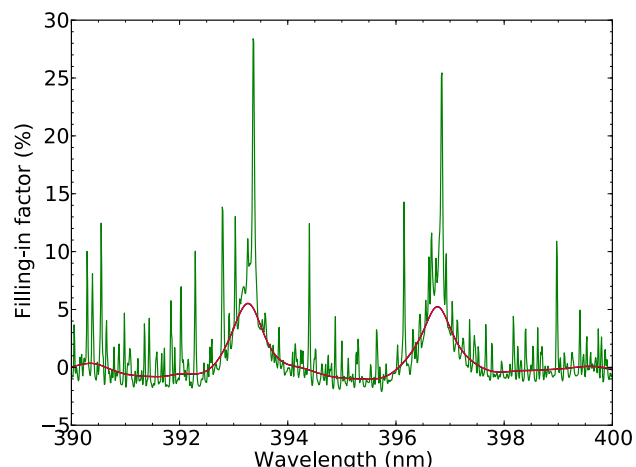


Fig. 2. The filling-in calculated from simulated irradiances at the Earth’s surface using an ET-spectrum with 0.01 nm resolution (green line), and ET-spectrum convolved with an instrument (the Bentham spectroradiometer in Garmisch-Partenkirchen with slit function FWHM of 0.5 nm, see section 4.1) response function prior to simulation at 0.05 nm resolution (red line). Simulations with ET-spectrum with 0.01 nm resolution and results convolved with an instrument spectral response function, and the ET-spectrum convolved with the instrument response function prior to simulation at 0.01 nm resolution (not shown), are indistinguishable from the red line on the present scale. The solar zenith angle is 75° and the surface albedo is 0.0.

3 Examples of RRS

Below the new RRS radiative transfer model is used to investigate the effects of clouds on DODs and filling-in factors.

3.1 Cloud top height

de Beek et al. (2001) showed how the differential optical depth varied with cloud top height for various cloud optical depth. Their Fig. 4 is reproduced in Fig. 3a (solid lines) for the same cloud optical depths and cloud top height. The cloud was taken to be 1 km thick in the vertical and moved upwards as the cloud top height increased. The DODs are derived from top of the atmosphere (TOA) upwelling radiances for zero viewing angle (nadir radiances). The dependence on the cloud optical depth and cloud top height are similar for the two models. Also shown in Fig. 3a are DODs for the cloud bottom fixed at 0.5 km and increasing cloud top height (dashed lines). For all cloud vertical thicknesses the DOD decreases with increasing cloud top height. As the cloud top height increases fewer photons make it down to the denser lower atmosphere due to scattering in the cloud. Hence, fewer photons experience RRS with increasing cloud top height. The shallow cloud (solid lines) is more effective in reducing the penetration of photons into the lower part of the atmosphere compared to the optically less dense extended cloud (dashed lines). Hence, RRS is lower for the shallow

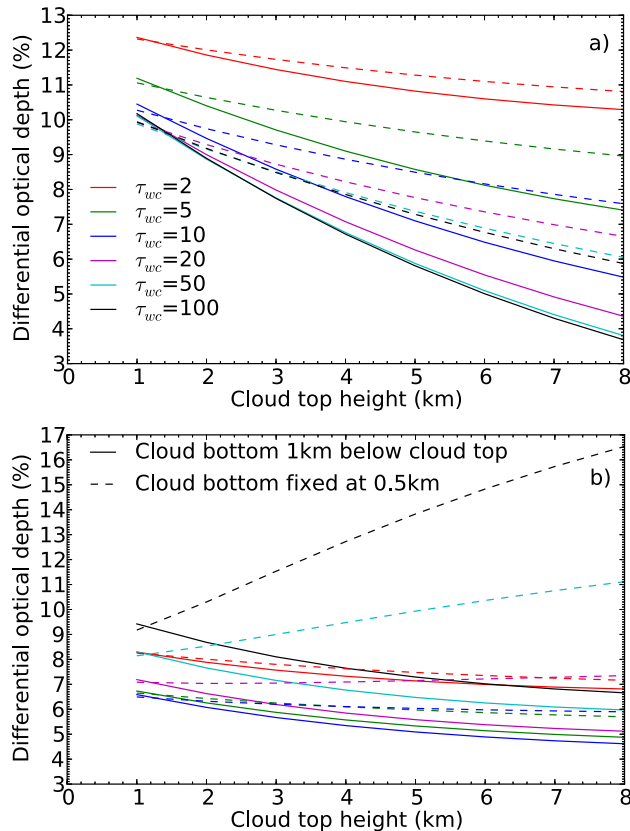


Fig. 3. The differential optical depth calculated (a) from top of the atmosphere nadir radiances, and (b) bottom of the atmosphere zenith radiances for a wavelength of 393.37 nm. The solar zenith angle is 52.9° and the surface albedo is 0.05. For the solid lines the cloud is 1 km thick in the vertical. For the dashed lines the cloud bottom is at 0.5 km and the cloud vertical extent increases as the cloud top height increases.

cloud, except for the case of lowest cloud top height. However, in this case the shallow cloud extends from the surface to 1 km while the extended cloud goes from 0.5 to 1.0 km. Thus, the behaviour is expected.

In Fig. 3b DODs calculated from bottom of the atmosphere (BOA) downwelling radiances for a 90° elevation angle (zenith radiances) are shown for the same clouds as in Fig. 3a. Generally the BOA DODs vary less with cloud top height than the TOA DODs. For the shallow cloud (solid lines) a decrease with increasing cloud top height is caused by decreased photon pathlengths within the cloud, and hence decreased likelihood for RRS, as the shallow cloud is moved upwards. For the extended cloud (dashed lines) a similar behaviour is seen for cloud optical depths less than 20. For the cloud optical depths of about 20 or larger, the DODs increase with increasing cloud top height. As the cloud optical depth increases fewer photons traverse the cloud from top to bottom. Those who do, are increasingly more likely to experi-

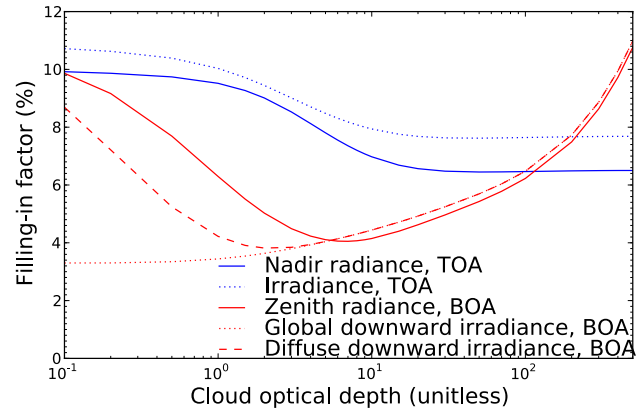


Fig. 4. The filling-in factor at 393.37 nm as a function of cloud optical depth for a solar zenith angle of 45° . Cloud bottom is at 1 km and cloud top at 2 km with the surface at 0.0 km and the albedo is 0.03. The ET-spectrum was convolved with a triangular response function with FWHM of 0.26 nm. The filling-in factors were calculated from top of the atmosphere (TOA) nadir radiances and diffuse upward irradiances, and bottom of the atmosphere (BOA) global (direct plus diffuse) and diffuse downward irradiances and zenith radiances.

ence RRS in the lower part of the atmosphere with increasing cloud optical depth when the extended cloud is present there compared to the shallow cloud. Thus, for extended clouds the likelihood of a RRS event increases with increasing optical depth. The results presented in Fig. 3a and b clearly demonstrate that both TOA and BOA DODs depend on the vertical extent and location of the cloud.

3.2 Cloud optical depth

The variation of FI with cloud optical depth is shown in Fig. 4 for a solar zenith angle of 45° . The cloud bottom is at 1 km and the cloud top at 2 km. The cloud optical depth is varied from 0 to 500. Although a cloud optical depth of 500 is physically unrealistic for a cloud extension of 1 km, this case is instructive since it closely approximates the idealized case of a semi-infinite bidirectionally reflecting medium. Filling-in factors are shown for TOA diffuse upward irradiance and nadir radiance (blue lines) and BOA global and diffuse irradiances and zenith radiance (red lines).

The TOA filling-in from the nadir radiance and diffuse upward irradiance (blue lines Fig. 4) decrease with increasing cloud optical depth. It starts to level off at optical depths between 10 and 20 and reaches values of 6.5 and 7.7 % respectively for a cloud optical depth $\tau_{wc} = 500$. A similar levelling for nadir radiance derived filling-in factors may be seen in the results of Fig. 4 de Beek et al. (2001) (see also Fig. 3a present paper).

The BOA FI factors from the zenith radiance and global downward irradiance show no sign of levelling off with increasing cloud optical depth (red lines Fig. 4). When the

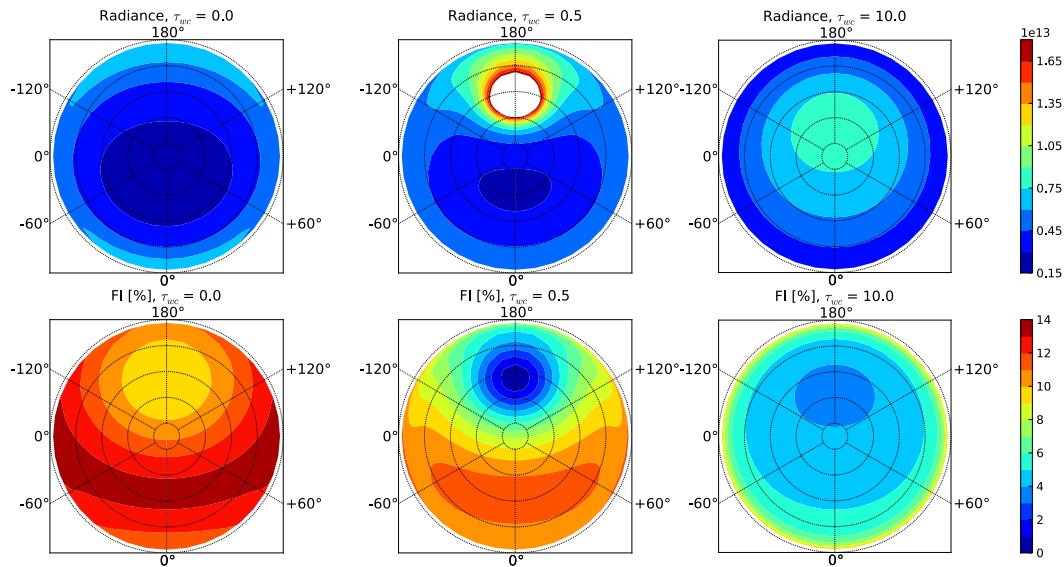


Fig. 5. The upper row shows the BOA radiances [photon/(s cm² nm sr)] at 393.37 nm for cloudless, $\tau_{wc} = 0.0$, and cloud optical depths of 0.5 and 10.0. The simulations were made for the same conditions as in Fig. 4. The lower row shows corresponding FI factors. The circles indicate polar angles of 10, 30, 50, 70, and 90° moving outwards. The azimuth angles are shown on the plots.

cloud optical thickness increases the cloud increasingly resembles a semi-infinite scattering medium. Thus, the path-length increase of photons backscattered into the upper hemisphere will level off and the filling-in factor behaves correspondingly at TOA. Below the cloud, the photon path length will increase as long as the cloud optical depth increases. A larger photon path length increases the chance for RRS. Hence, the FI factors increase with increased cloud optical depth for surface based zenith-viewing and global irradiance instruments. Obviously, the absolute zenith radiance and global downward irradiance are rather small for optically very thick clouds, see for example Fig. 9 below.

The zenith radiance and global downward irradiance derived filling-in factors at the BOA behave very differently for small cloud optical depths (red lines Fig. 4). The zenith radiance-based FI factor have a minimum of 4 % for a cloud optical depth slightly less than 10 and increases for smaller optical depths to the cloudless value of 10.8 %. The filling-in factor from the global downward irradiance at the BOA exhibits no minimum, but decreases with decreasing cloud optical depth. The global irradiance has two components, the direct and the diffuse downward irradiance. The relative magnitude of the direct irradiance increases with decreasing cloud optical depth. As the direct beam does not contribute to the filling-in factor, the filling-in factor based on the global irradiance will decrease with decreasing cloud optical depth. This is also readily seen from the filling-in factor calculated from the diffuse downwelling irradiance (dashed red line, Fig. 4).

To further illustrate the behaviour of the filling-in factor at the BOA, the downwelling radiance is shown in the up-

per row in Fig. 5 for a cloudless situation and two cloud cases with optical depths of 0.5 and 10.0. The direct beam contribution is not included in the figure. The corresponding filling-in factors are shown in the bottom row. For the cloudless sky the smooth Rayleigh and Raman phase function gives a correspondingly smooth radiance field (upper left plot, Fig. 5). For the optically thin cloud (upper center plot, Fig. 5) the strongly forward peaked phase function of water droplets gives a correspondingly strong maximum in the direction of the sun. For the optically thicker cloud, this maximum is no longer seen, as multiple scattering within the cloud has removed nearly all original directional information from the photons (upper right plot, Fig. 5). The filling-in plots (lower row Fig. 5) reflects the behaviour of the radiances. The filling-in factors have minima in the direction of the sun for the cloudless and optically thin cloud. For the optically thicker cloud the minimum is less pronounced and slightly offset towards the zenith as similar for the radiance.

3.3 Vertical profiles of filling-in factors

Similar to the model of Spurr et al. (2008), the present model can calculate the radiation field anywhere in the atmosphere. In Fig. 6 vertical profiles of the filling-in factor are shown for the same cloud as in Spurr et al. (2008, Fig. 8). The cloud layer was between 2 and 3 km, with a single scattering albedo of 0.9999 and a Henyey-Greenstein phase function with asymmetry factor 0.8. The solar zenith angle was set to 45°. Spurr et al. (2008) displayed the filling-in for several wavelengths and cloud optical depths. Here the filling-in is shown for one wavelength, 393.37 nm, and for

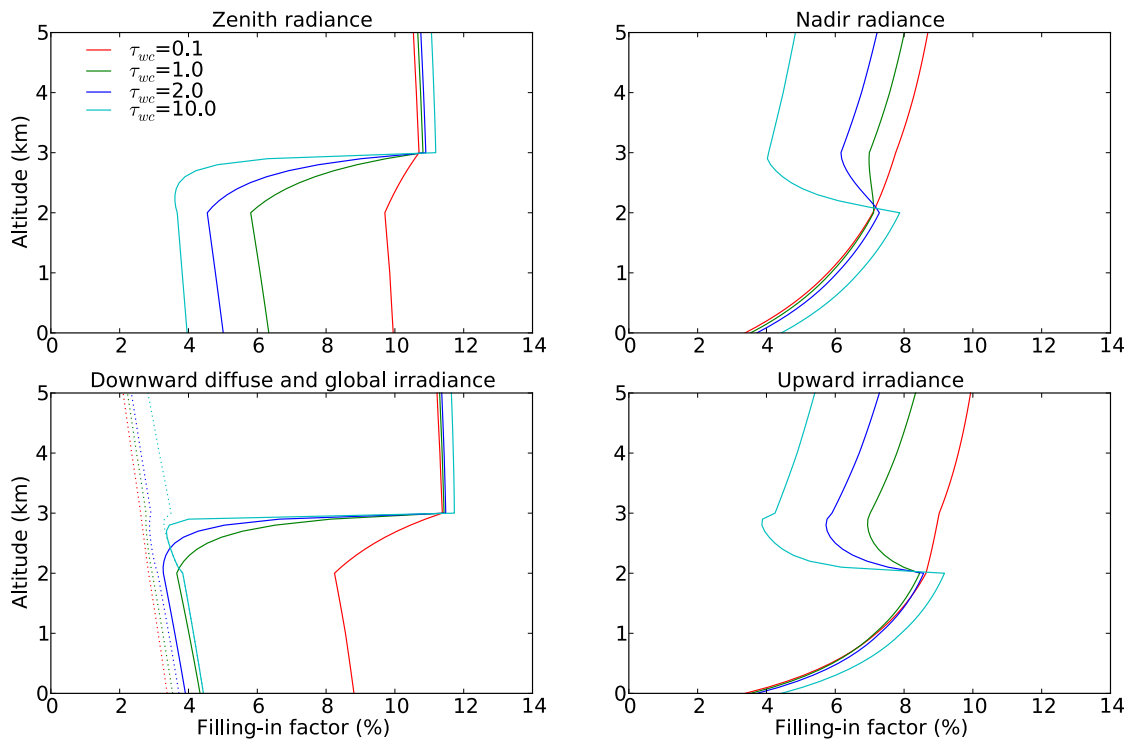


Fig. 6. Profiles of the filling-in factor as calculated from radiances (top row) and irradiances (bottom row). Solid lines represent filling-in factors calculated from radiances (upper row) and diffuse upward and downward irradiances (lower row). Dashed lines are filling-in factors calculated from the global (direct plus diffuse downward) irradiance. As in Spurr et al. (2008) the cloud layer was located between 2 and 3 km and the surface at 0.0 km. Altitude resolution 0.1 km.

both irradiances and radiances. Filling-in factor profiles are shown for cloud optical depths of 0.1, 1.0, 2.0 and 10.0 as calculated from both radiances (upper row Fig. 6) and irradiances (lower row Fig. 6). The results for the diffuse downward and upward irradiance based filling-in irradiance factors (solid lines in the lower row Fig. 6) agree reasonably well with those presented by Spurr et al. (2008, Fig. 8).

Concerning the downwelling radiation it is clear that the cloud has little impact on the filling-in factor calculated from the global (direct plus diffuse) irradiance (dashed lines, lower row, left plot Fig. 6). The filling-in factors calculated from the nadir radiance and the upward irradiance clearly exhibit the signature of the cloud. For the global downwelling field, the radiation above the cloud is dominated by the direct beam, hence the filling-in is small. In and below the cloud the radiation field becomes diffuse and the global filling-in approaches the diffuse filling-in for clouds of optical thickness greater than 1. For the upwelling irradiance filling-in factor the clouds decrease the filling-in above the cloud. This is caused by a decrease in the photon pathlength due to the presence of the cloud.

The behaviour of the filling-in factors calculated from the zenith and nadir radiances, upper row Fig. 6, is similar to that calculated from the irradiances, lower row Fig. 6. To un-

derstand these results it is instructive to look at the radiance in the solar principal plane at various altitudes below, inside and above the cloud. Fig. 7 shows the radiances calculated with and without Raman scattering at BOA, 1.9, 2.1, 2.3, 2.5, 2.7, 2.9, and 3.1 km, and at TOA. The angular distribution of diffuse radiation changes dramatically with altitude and especially within the cloud. At the TOA (upper left plot Fig. 7) there is no downwelling diffuse radiation and the upwelling diffuse radiation is fairly homogeneous. Just above the cloud top, at 3.1 km, a majority of the diffuse radiation is in the upward direction, but some radiation is also scattered downwards by the above atmosphere. Once inside the cloud the picture changes dramatically. The strongly forward scattering water droplets gives rise to a strong lobe in the direction of the direct sun ray. As one moves deeper into the cloud the lobe broadens due to multiple scattering. But at the bottom of the cloud there is still an asymmetry in the radiance field. Thus, within a cloud of optical depth 10, there should be little problem to distinguish up from down based on the diffuse radiation field. Due to the low surface albedo (0.05), there is little diffuse upwelling radiation below the cloud. At the BOA there is still some asymmetry in the radiation field.

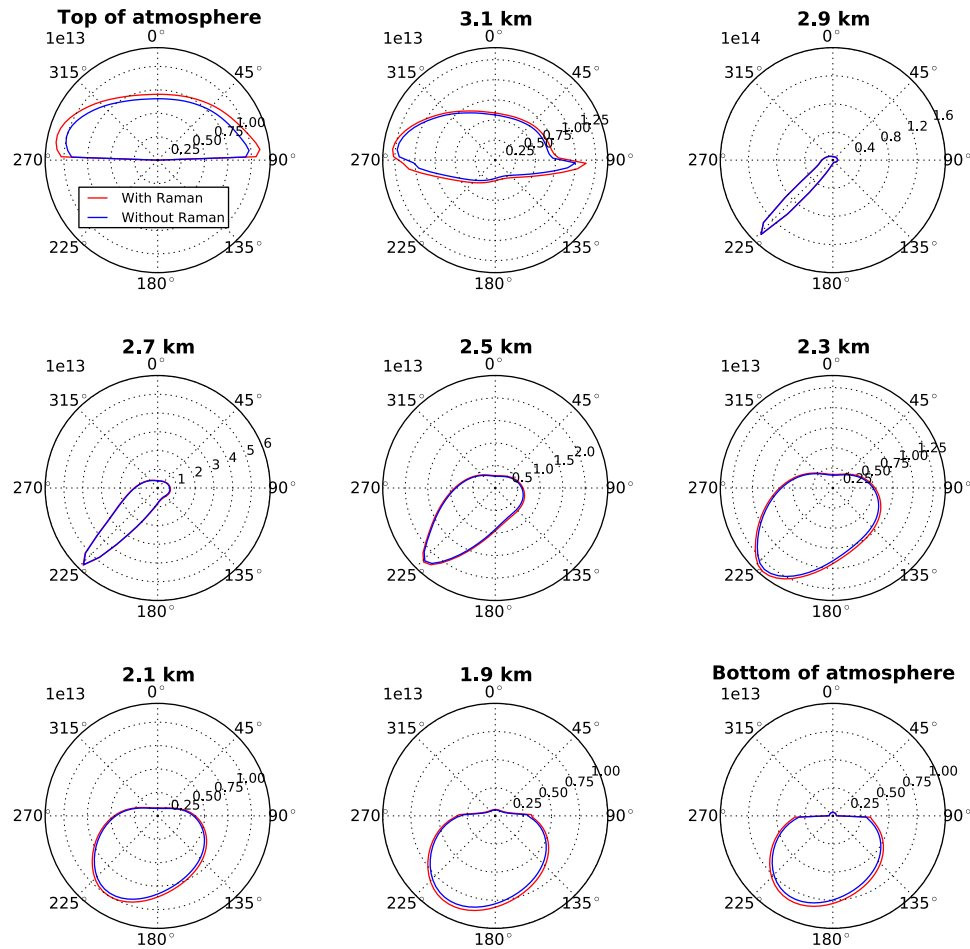


Fig. 7. The radiance [photons/(s cm² nm sr)] in the solar principal plane for various altitudes. The solar principal plane is defined to be the plane laid out by the incoming solar beam with azimuth angle $\Phi_0 = 180^\circ$ and radiation scattered in the forward direction, $\Phi = 0^\circ$. The polar angle gives the direction of the radiation in the plane. A polar angle of 0° gives radiation travelling in the zenith direction. The sun is incident at 45° . The atmospheric conditions are as in Fig. 6 with a cloud of optical depth of 10 located between 2 and 3 km. Note that the scales on the various plots differ.

From the radiances with and without RRS, filling-in factors may be calculated as shown in Fig. 8. The angular behaviour of the filling-in reflects the pathlength travelled by the individual photons. In the direction of the direct sun ray near the top of the cloud, some photons have been scattered once and thus the chance of RRS is small. For the other directions, the photons have increasingly been scattered several times and hence the chance of RRS increases. This is seen in the correspondingly large filling-in factors in the upper hemisphere within the cloud. The filling-in varies considerably with viewing angle and the minima at 2.5, 2.7 and 2.9 km, in the direction of the direct sun ray stand out in particular. Results are shown for one solar zenith angle. Clearly, the picture will be different for other solar zenith angles and cloud situations. Specifically, within the upper part of the cloud the radiance calculated filling-in will vary with solar zenith angle.

4 Comparison with surface measurements

To demonstrate the spectral behaviour of RRS effect, model simulations were compared with two different experimental cases. The first case involved a thunderstorm over Garmisch-Partenkirchen, Germany (47.48° N, 11.07° E, and 730 m above sea level, Mayer et al. (1998)). The second case from Nea Michinanona, Greece (40.28° N, 22.51° E, and 30 m above sea level), utilizes measurements made under a heavy aerosol load (Kylling et al., 2003). For both cases, input parameters for model simulations were obtained from independent measurements. They represent the most complete knowledge of input parameters available for the studied cases. Thus, no tuning of input parameters was performed for this paper.

For the simulation of the measurements, the high-resolution ET spectrum was convolved with the respective

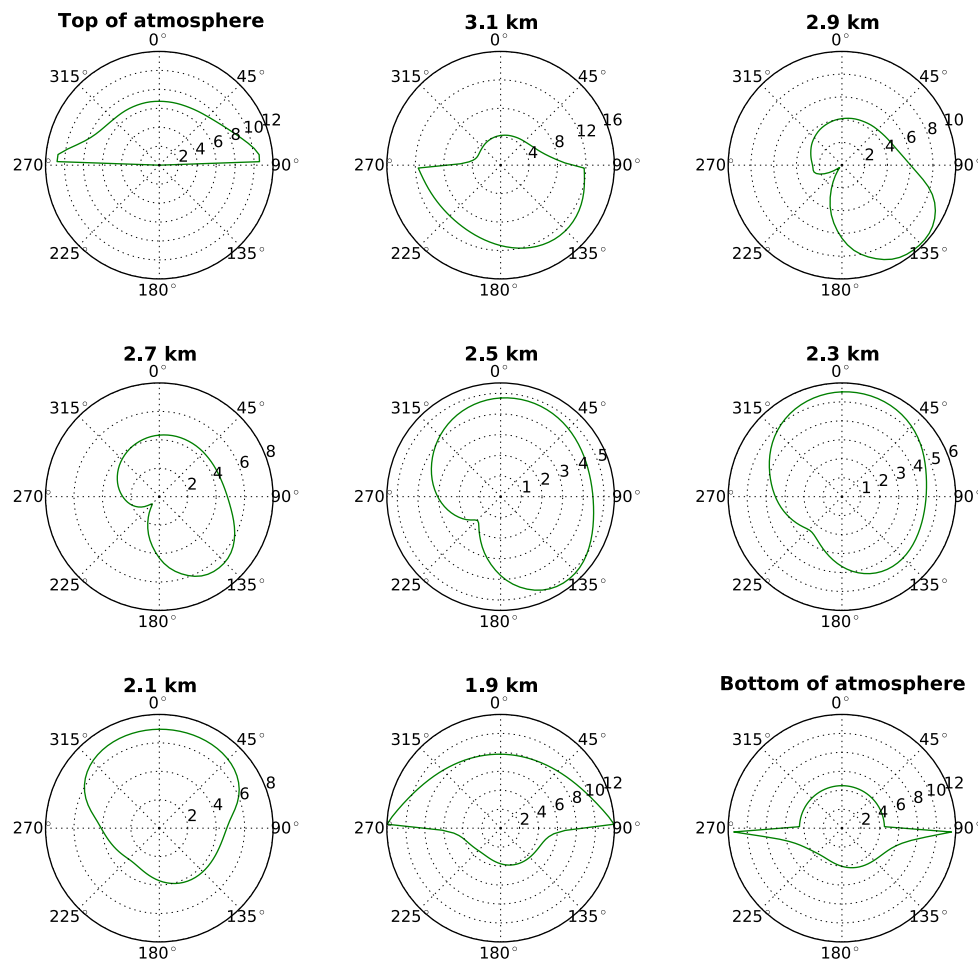


Fig. 8. The filling-in factor [%] in the principal plane for various altitudes. The polar angle gives the direction of the radiation. Calculated from the radiances in Fig. 7. Note that the scales on the various plots differ.

instrument response function and regridded to 0.05 nm resolution. On-site measurements of atmospheric profiles were not available. Instead, standard profiles from Anderson et al. (1986) were used. To minimize uncertainties caused by missing knowledge of the ozone profile, the wavelength region 340–410 nm, where ozone absorption is small, was investigated. Absorption by ozone was included using the cross section of Daumont et al. (1992), while the absorption cross sections for O₄ were taken from Greenblatt et al. (1990). Furthermore, absorption by NO₂ (Burrows et al., 1998) was included with a column amount of 0.22 Dobson units.

Both measurements are oversampled by factor of 2 in accordance with the Nyquist-theorem. When spectra are resampled into the same wavelength grid higher frequency information may be aliased into the spectrum (Chance et al., 2005). The wavelength accuracy for the measured spectra are about 0.01–0.02 nm. In the worst case this corresponds to a shift of 0.02 nm which translates into an interpolation error in the DODs of about 0.01–0.02 (Roscoe et al., 1996).

4.1 Thunderstorm case

The thunderstorm took place over Garmisch-Partenkirchen on 19 June 1994, and has been described by Mayer et al. (1998). The sky was relatively cloudless in the morning allowing the recording of a reference spectrum. A large thunderstorm developed during the day with a maximum optical depth around 14:10 UTC. The cloudless, 07:46 UTC, and fully thunderstorm, 14:10 UTC, situations were simulated. Model input data were taken from Mayer et al. (1998, Table 1): For the fully developed thunderstorm at 14:10 UTC the solar zenith angle was 33°. The cloud was assumed to extend from 1 to 9 km with optical depth $\tau_{wc} = 340$. The effective droplet radius was set to 10.5 μm and the water cloud optical properties were calculated from the parameterization of Hu and Stamnes (1993). In addition sensitivity studies were made with optical properties from Mie calculations based on Mie water cloud optical property tables available from <http://www.libradtran.org>.

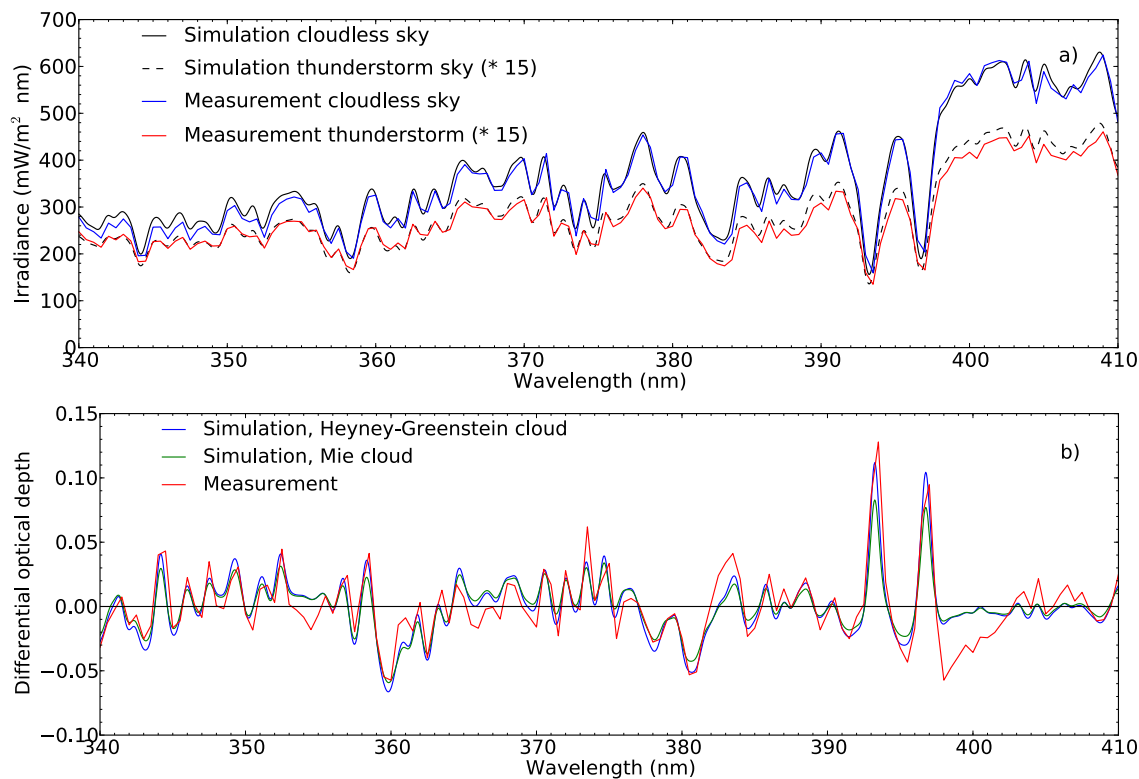


Fig. 9. (a) The measured (red and blue lines) and simulated (black line) spectra under cloudless (blue) and thunderstorm (red) situations. The measured and modelled thunderstorm spectra have been multiplied by a factor of 15. (b) The measured and simulated DOD. Simulations with both a Henyey-Greenstein phase function (blue) and an exact Mie phase function (green) are shown. The input parameters to the model simulation are described in the text.

For the cloudless case at 07:46 UTC the solar zenith angle was 57°. The wavelength dependent aerosol optical depth, τ_{aero} , was calculated using the Ångström formula, $\tau_{\text{aero}} = \beta\lambda^{-\alpha}$, with $\alpha = 1.147$ and $\beta = 0.20$, as determined from direct sun measurements by the same instrument. The aerosol single scattering albedo was set to 0.95 and the aerosol asymmetry factor to 0.7. The aerosol was included in both the cloudy and cloudless situations.

It is noted that both the cloud geometry and the inclusion of aerosol for the cloudy situation are somewhat arbitrary. Mayer et al. (1998) used an earlier version of the libradtran model to analyse the effects of varying the aerosol and cloud optical depths for the cloudy situation. The values adopted here, while not unique, are similar to those derived from the model/measurement comparison described in Mayer et al. (1998). For both situations a Lambertian surface albedo of 0.03 was assumed and the US midlatitude summer atmosphere was adopted (Anderson et al., 1986).

The measurement platform was located at the Fraunhofer Institute, Garmisch-Partenkirchen, Germany. The system for measuring spectral UV irradiance comprises a Bentham double monochromator DTM 300 with a photomultiplier as detector. Spectra of global irradiance were measured with a quartz cosine diffuser, and direct spectral irradiance

was measured with narrow field-of-view entrance optics automatically aligned to the Sun. Calibrations were carried out on a weekly basis using 100 W tungsten-halogen standard lamps traceable to the Physikalisch Technische Bundesanstalt (PTB, Braunschweig, Germany). The instrument has a slit width of 0.5 nm (FWHM) and a step width of 0.25 nm between 285 and 410 nm. For this study a very high wavelength alignment is required. Therefore the wavelength accuracy (uncertainty typically 0.05 nm, carefully maintained by a spectral calculation with Mercury lamps) was further improved with the following procedure: The wavelength-dependent wavelength shift was determined by cross-correlation of the measured spectrum and a model calculation based on the ATLAS3 spectrum. The wavelength shift was then added to each individual spectral point and finally the spectrum was spline interpolated to a regular 0.25 nm grid. The remaining wavelength uncertainty was of the order of 0.01–0.02 nm. It is noted that for the spectrum recorded during the thunderstorm, concurrent recordings by an illuminance meter showed that the illuminance was stable within $\pm 5\%$ ($\pm 1\sigma$) for the duration of the scan, thus indicating that no rapid changes in the cloud took place during the scan.

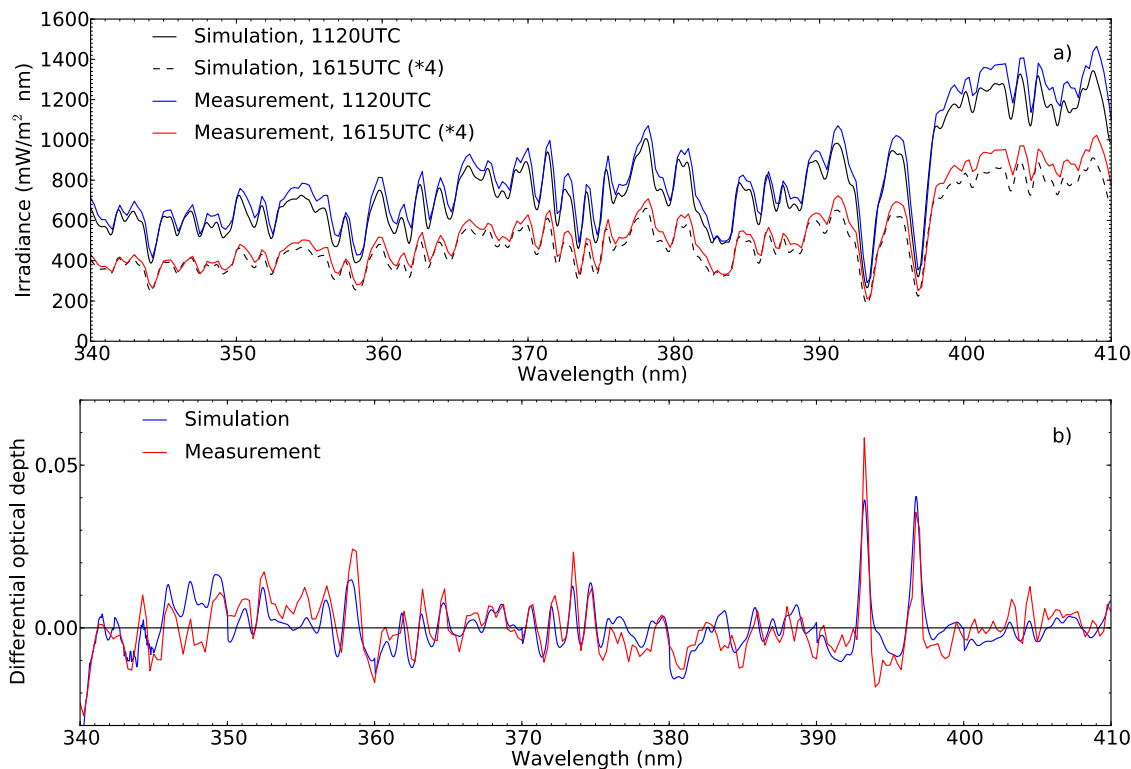


Fig. 10. (a) The measured spectra at 11:20 UTC (blue line) and 16:15 UTC (red line). The corresponding model simulations are shown in black. (b) The measured (red line) and simulated (blue line) DODs. Note difference in y-axis scale from Fig. 9b. The input parameters to the model simulation are described in the text.

Figure 9a shows the measured and modelled downwelling global (direct plus diffuse) irradiances for the cloudless and thunderstorm cases (solid lines). The thunderstorm spectra have been multiplied by a factor of 15 for better visualization. Mayer et al. (1998) compared a measured cloudless spectrum recorded at a similar solar zenith angle, but on another day, with the thunderstorm cloud spectrum and found that the thunderstorm irradiance was reduced to about 2.5 % of its cloudless value.

For comparison of measured and modelled RRS effects the DOD is calculated. The cloudless spectrum is taken as E_{ref} and E is the thunderstorm spectrum. The DODs calculated from the measured and calculated spectra are shown in Fig. 9b. The agreement between the measured and calculated DODs is better than 0.01 with only few exceptions. These may partly be caused by instrumental noise which was smaller than 1 % corresponding roughly to an uncertainty in the DOD of 0.01.

At the time of Mayer et al. (1998) it was quite common to use the Henyey-Greenstein phase function, e.g. as in the parameterization by Hu and Stammes (1993), to describe cloud optical properties for irradiance calculations. For irradiances, differences between results computed with Henyey-Greenstein and Mie-calculated phase functions may be sub-

stantial. To investigate the effects on irradiances, the simulations were repeated with phase functions from Mie theory calculations. The cloud droplet sizes were assumed to be described by a gamma-distribution with $\alpha = 7$ and the effective radius $r_{\text{eff}} = 10 \mu\text{m}$. For more details see Emde et al. (2010, Sect. 2.3). The Henyey-Greenstein phase function was used while deriving the cloud optical depth of 340. Changing to the Mie phase function will also affect the derived cloud optical depth. Simulations with the Mie phase function were made both with the cloud optical depth of 340 and a value of 332 which was derived using the Mie phase function. Both simulations changed the DOD in a similar manner. The resulting DOD is shown in green in Fig. 9b. Using the exact phase function reduces the DOD by up to 25 % for the investigated case. There are two reasons for this. The effective pathlength of the photons may be calculated as explained in Sect. 2. For photons that travel through the cloud, the pathlength increases by about 2 % when changing from the Henyey-Greenstein phase function to the Mie phase function. In the model atmosphere, absorbing aerosols are also present in the cloud. Thus, the increase in pathlength leads to increased absorption of photons and hence less Raman scattering. By excluding aerosols there is still a difference in the DODs calculated using either the Henyey-Greenstein phase

function or the Mie phase function, with a smaller DOD for the Mie phase function. It is estimated that for the present case the aerosol accounts for about two thirds of the reduction in the DOD. The remaining difference is caused by differences in the phase functions. The Mie phase function has a larger back-scattering part, see for example Mayer and Kylling (2005, Fig. 6), thus less photons make it through the cloud. This implies that less photons are available for scattering into the wavelength of interest compared to a Henyey-Greenstein phase function. Hence, the DOD is further reduced for the Mie phase function.

4.2 Aerosol case

The aerosol case was based on a situation that occurred during the Actinic flux determination from measurements of irradiance (ADMIRA) measurement campaign, August 2000 at Nea Michaniona, Greece (Webb et al., 2002). Two irradiance spectra on the 5th of August were simulated. The first spectrum was measured at 11:20 UTC and the solar zenith angle varied from 25.69° at 340 nm to 25.82° at 410 nm. The aerosol optical depth was estimated from direct sun measurements by the same instrument and reported in terms of Ångström coefficients. For the first spectrum the Ångström coefficients were $\alpha = 2.14$ and $\beta = 0.038$ giving $\tau_{\text{aero}}(\lambda = 400 \text{ nm}) = 0.27$. The second spectrum was measured at 1615 UTC and the solar zenith angle varied from 76.08° at 340 nm to 76.52° at 410 nm, with $\alpha = 2.05$ and $\beta = 0.027$, giving $\tau_{\text{aero}}(\lambda = 400 \text{ nm}) = 0.18$. The Lambertian surface albedo was set to a constant value of 0.03, the value adopted by Kylling et al. (1998) for a similar situation. The US standard atmosphere (Anderson et al., 1986) was used and the aerosol single scattering albedo and asymmetry factor were taken from the rural spring-summer parameterisation of Shettle (1989). In this parameterisation the aerosol single scattering albedo and asymmetry factor vary with altitude and wavelength. The single scattering albedo takes on values between 0.94–0.98 while the asymmetry factor is about 0.67–0.70.

The spectra for the aerosol case were measured with a Bentham DTM300 double monochromator spectroradiometer (Blumthaler et al., 2008). For these measurements the instrument was equipped with gratings with 2400 lines per mm, resulting in a slit width of 0.48 nm (FWHM). The spectra were recorded with a step size of 0.25 nm.

The spectral calibration was routinely checked against the structure of the Fraunhofer lines, which resulted in an overall absolute uncertainty of the spectral alignment of less than 0.1 nm. The precision of the spectral alignment is better than 0.05 nm. For further improvement of the spectral alignment, the spectra were corrected using the ShicRIVM algorithm Slaper et al. (1995), which yields a reproducibility of the wavelength setting of the spectra on the level of 0.01 nm.

The absolute calibration is based on a 1000 W halogen lamp, traceable to the Physikalisch Technische Bundesanstalt

(PTB, Braunschweig, Germany). The integration time when reading out the photomultiplier current is adapted to the absolute level of the signal in order to achieve a good signal to noise ratio at each wavelength. For wavelengths above 340 nm this is usually 20 ms, which leads to a statistical noise in the order of 0.3 %. The overall spectral noise, when comparing two consecutive spectra in the wavelength range between 340 nm and 410 nm is in the order of 0.5 %.

The measured and simulated aerosol spectra are shown in Fig. 10a. The measured and modelled DODs for the aerosol case are shown in Fig. 10d. As for the thunderstorm case the measured and modelled DODs show the same spectral behaviour. The effect of RRS is significantly smaller for the aerosol case than for the thunderstorm case. This is so even if in the thunderstorm case the direct optical path increases by a factor of 1.54 when the solar zenith angle increases from 33° to 57° , while for the aerosol case the pathlength increases by 3.71 when the solar zenith angle increases from 26° to 76° . The larger differential optical depth for the thunderstorm case is caused by multiple scattering within the cloud which increases the photon pathlength and thus the likelihood of a Raman scattering event. It is noted that the filling-in may be attributed to either changes in the aerosol content or the solar zenith angle between the spectra. Simulations were made of the two spectra with varying aerosol content but similar solar zenith angle, and similar aerosol content but different solar zenith angles. The simulations clearly demonstrated that the filling-in is due to the difference in the solar zenith angle between the two spectra.

5 Conclusions

A new radiative transfer model including first-order RRS has been presented. The model is based on a reimplementation in the C computer language of the discrete ordinate radiative transfer (DISORT) algorithm. The solution allows the computation of the radiation field including RRS in pseudo-spherical geometry, at any altitude in the atmosphere and at any viewing angle. An interpolation scheme allows speed-up in computer time between 10–100 depending on the application. The model has been used to investigate the interaction of clouds and RRS, and the effect on filling-in factors and differential optical depths. It was found that filling-in factors calculated from BOA irradiances and nadir radiances increase with increasing cloud optical depth due to the increase in photon path lengths. Polar plots of radiances and filling-in factors from radiances exhibit strong asymmetries deep inside and below clouds. Differential optical depths calculated with the model shows the same spectral dependence as measurements of the same quantity for both thunderstorm and aerosol loaded cases.

The radiative transfer model, including first-order RRS, is available from <http://www.libradtran.org>.

Acknowledgement Model development was supported by the ESA-funded project ESASLight, ESTEC contract AO/1-5433/07/NL/HE. We give our thanks to the reviewers for comments and suggestions that greatly helped to improve the paper.

Edited by: M. Van Roozendael

References

- Anderson, G., Clough, S., Kneizys, F., Chetwynd, J., and Shettle, E.: AFGL atmospheric constituent profiles (0–120 km), Tech. Rep. AFGL-TR-86-0110 Air Force Geophys. Lab., Hanscom Air Force Base, Bedford, Mass., 1986.
- Blumthaler, M., Schallhart, B., Schwarzmüller, M., McKenzie, R., Johnston, P., Kotkamp, M., and Shiona, H.: Spectral UV Measurements of Global Irradiance, Solar Radiance, and Actinic Flux in New Zealand: Intercomparison between Instruments and Model Calculations, *J. Atmos. Ocean. Technol.*, 25, 945–958, 2008.
- Buras, R., Dowling, T., and Emde, C.: New secondary-scattering correction in DISORT with increased efficiency for forward scattering, *J. Quant. Spectrosc. Ra.*, 2028–2034, doi:10.1016/j.jqsrt.2011.03.019, 2011.
- Burrows, J. P., Dehn, A., Deters, B., Himmelmann, S., Richter, A., Voigt, S., and Orphal, J.: Atmospheric remote-sensing reference data from GOME: Part 1. Temperature-dependent absorption cross sections of NO₂ in the 231–794 nm range, *J. Quant. Spectrosc. Ra.*, 60, 1025–1031, 1998.
- Chance, K. V. and Spurr, R. J. D.: Ring effect studies: Rayleigh scattering including molecular parameters for rotational Raman scattering, and the Fraunhofer spectrum, *Appl. Opt.*, 36, 5224–5230, 1997.
- Chance, K., Kurosu, T. P., and Sioris, C. E.: Undersampling correction for array detector-based satellite spectrometers, *Appl. Opt.*, 44, 1296–1304, 2005.
- Chandrasekhar, S.: Radiative Transfer, Dover, Mineola, N. Y., ISBN 0-486-60590-6, 1960.
- Clough, S. A., Shephard, M. W., Mlawer, E. J., Delamere, J. S., Iacono, M. J., Cady-Pereira, K., Boukabara, S., and Brown, P. D.: Atmospheric radiative transfer modeling: a summary of the AER codes, *J. Quant. Spectrosc. Ra.*, 91, 233–244, 2005.
- Dahlback, A. and Stammes, K.: A new spherical model for computing the radiation field available for photolysis and heating at twilight, *Planet. Space Sci.*, 39, 671–683, 1991.
- Daumont, D., Brion, J., Charbonnier, J., and Malicet, J.: Ozone UV spectroscopy I: Absorption cross-sections at room temperature, *J. Atmos. Chem.*, 15, 145–155, doi:10.1007/BF00053756, 1992.
- de Beek, R., Vountas, M., Rozanov, V. V., Richter, A., and Burrows, J. P.: The Ring effect in the cloudy atmosphere, *Geophys. Res. Lett.*, 28, 721–724, 2001.
- de Haan, J. F.: Accounting for Raman scattering in DOAS, Tech. rep., SN-OMIE-KNMI-409, 2003.
- Emde, C., Buras, R., Mayer, B., and Blumthaler, M.: The impact of aerosols on polarized sky radiance: model development, validation, and applications, *Atmos. Chem. Phys.*, 10, 383–396, doi:10.5194/acp-10-383-2010, 2010.
- Fontenla, J., White, O. R., Fox, P. A., Avrett, E. H., and Kurucz, R. L.: Calculation of solar irradiances. I. Synthesis of the solar spectrum, *The Astrophys. J.*, 518, 480–499, 1999.
- Grainger, J. F. and Ring, J.: Anomalous Fraunhofer line profiles, *Nature*, 193, 762, 1962.
- Greenblatt, G. D., Orlando, J. J., Burkholder, J. B., and Ravishankara, A. R.: Absorption measurements of oxygen between 330 and 1140 nm, *J. Geophys. Res.*, 95, 18577–18582, 1990.
- Gurlit, W., Bösch, H., Bovensmann, H., Burrows, J. P., Butz, A., Camy-Peyret, C., Dorf, M., Gerilowski, K., Lindner, A., Noël, S., Platt, U., Weidner, F., and Pfeilsticker, K.: The UV-A and visible solar irradiance spectrum: inter-comparison of absolutely calibrated, spectrally medium resolution solar irradiance spectra from balloon- and satellite-borne measurements, *Atmos. Chem. Phys.*, 5, 1879–1890, doi:10.5194/acp-5-1879-2005, 2005.
- Hasekamp, O. P. and Landgraf, J.: Ozone profile retrieval from backscattered ultraviolet radiances: The inverse problem solved by regularization, *J. Geophys. Res.*, 106, 8077–8088, 2001.
- Hoogen, R., Rozanov, V. V., and Burrows, J. P.: Ozone profiles from GOME satellite data: Algorithm description and first validation, *J. Geophys. Res.*, 104, 8263–8280, 1999.
- Hu, Y. X. and Stammes, K.: An accurate parameterization of the radiative properties of water clouds suitable for use in climate models, *J. Climate*, 6, 728–742, 1993.
- Joiner, J. and Bhartia, P. K.: The determination of cloud pressures from rotational Raman scattering in satellite backscatter ultraviolet measurements, *J. Geophys. Res.*, 100, 23019–23026, 1995.
- Joiner, J. and Vasilkov, A. P.: First results from the OMI Rotational Raman scattering cloud pressure algorithm, *IEEE T. Geosci. Remote Sens.*, 44, 1272–1282, 2006.
- Joiner, J., Bhartia, P. K., Cebula, R. P., Hilsenrath, E., McPeters, R. D., and Park, H.: Rotational Raman scattering (Ring effect) in satellite backscatter ultraviolet measurements, *Appl. Opt.*, 21, 4513–4525, 1995.
- Joiner, J., Vasilkov, A. P., Flittner, D. E., Gleason, J. F., and Bhartia, P. K.: Retrieval of cloud pressure and oceanic chlorophyll content using Raman scattering in GOME ultraviolet spectra, *J. Geophys. Res.*, 109, doi:10.1029/2003JD003698, 2004.
- Joiner, J., Vasilkov, A. P., Bhartia, P. K., Wind, G., Platnick, S., and Menzel, W. P.: Detection of multi-layer and vertically-extended clouds using A-train sensors, *Atmos. Meas. Tech.*, 3, 233–247, doi:10.5194/amt-3-233-2010, 2010.
- Kattawar, G. W., Young, A. T., and Humphreys, T. J.: Inelastic scattering in planetary atmospheres. I. The Ring effect, without aerosols, *The Astrophys. J.*, 243, 1049–1057, 1981.
- Kurucz, R. L.: Synthetic infrared spectra, in: *Infrared Solar Physics*, edited by: Rabin, D. and Jefferies, J., IAU Symp. 154, Kluwer, Acad., Norwell, MA, 1992.
- Kylling, A. and Stammes, K.: Efficient yet accurate solution of the linear transport equation in the presence of internal sources: the exponential-linear-in-depth approximation, *J. Com. Phys.*, 102, 265–276, 1992.
- Kylling, A., Bais, A. F., Blumthaler, M., Schreder, J., Zerefos, C. S., and Kosmidis, E.: Effect of aerosols on solar UV irradiances during the Photochemical Activity and Solar Ultraviolet Radiation campaign, *J. Geophys. Res.*, 103, 26051–26060, 1998.
- Kylling, A., Webb, A. R., Bais, A. F., Blumthaler, M., Scmitt, R., Thiel, S., Kazantzidis, A., Kift, R., Misslbeck, M., Schallhart, B., Schreder, J., Topaloglou, C., Kazadzis, S., and Rimmer, J.: Actinic flux determination from measurements of irradiance, *J. Geophys. Res.*, 108, 4506 (D16), doi:10.1029/2002JD003236, 2003.

- 2003.
- Landgraf, J., Hasekamp, O. P., van Deelen, R., and Aben, I.: Rotational Raman scattering of polarized light in the Earth atmosphere: a vector radiative transfer model using the radiative transfer perturbation theory approach, *J. Quant. Spectrosc. Ra.*, 87, 399–433, 2004.
- Lide, D.: Crc Handbook of Chemistry and Physics, 90th Edition, CRC, Boca Raton, 2009.
- Mayer, B. and Kylling, A.: Technical note: The libRadtran software package for radiative transfer calculations – description and examples of use, *Atmos. Chem. Phys.*, 5, 1855–1877, doi:10.5194/acp-5-1855-2005, 2005.
- Mayer, B., Kylling, A., Madronich, S., and Seckmeyer, G.: Enhanced absorption of UV radiation due to multiple scattering in clouds: Experimental evidence and theoretical explanation, *J. Geophys. Res.*, 103, 31241–31254, 1998.
- Nakajima, T. and Tanaka, M.: Algorithms for radiative intensity calculations in moderately thick atmospheres using a truncation approximation, *J. Quant. Spectrosc. Ra.*, 40, 51–69, 1988.
- Roscoe, H. K., Fish, D. J., and Jones, R. L.: Interpolation errors in UV-visible spectroscopy for stratospheric sensing: implications for sensitivity, spectral resolution, and spectral range, *Appl. Opt.*, 35, 427–432, 1996.
- Shettle, E. P.: Models of aerosols, clouds and precipitation for atmospheric propagation studies, paper presented at Conference on Atmospheric Propagation in the UV, Visible, IR and MM-Region and Related System Aspects, NATO Adv. Group for Aerosp. Res. and Dev., Copenhagen, 1989.
- Slaper, H., Reinen, H. A. J. M., Blumthaler, M., Huber, M., and Kuik, F.: Comparing ground-level spectrally resolved solar UV measurements using various instruments: A technique resolving effects of wavelengths shift and slit width, *Geophys. Res. Lett.*, 22, 2721–2724, 1995.
- Solomon, S., Schmeltekopf, A. L., and Sanders, R. W.: On the interpretation of zenith sky absorption measurements, *J. Geophys. Res.*, 92, 8311–8319, 1987.
- Spurr, R., de Haan, J. D., van Oss, R., and Vasilkov, A.: Discrete ordinate radiative transfer in a stratified medium with first order rotational Raman scattering, *J. Quant. Spectrosc. Ra.*, 109, 404–425, 2008.
- Stamnes, K.: The Theory of Multiple Scattering of Radiation in Plane Parallel Atmospheres, *Rev. Geophys.*, 24, 299–310, 1986.
- Stamnes, K. and Swanson, R. A.: A New Look at the Discrete Ordinate Method for Radiative Transfer Calculations in Anisotropically Scattering Atmospheres, *J. Atmos. Sci.*, 38, 387–399, 1981.
- Stamnes, K., Tsay, S.-C., Wiscombe, W., and Jayaweera, K.: Numerically stable algorithm for discrete-ordinate-method radiative transfer in multiple scattering and emitting layered media, *Appl. Opt.*, 27, 2502–2509, 1988.
- van Deelen, R., Landgraf, J., and Aben, I.: Multiple elastic and inelastic light scattering in the Earth's atmosphere: a doubling-adding method to include rotational Raman scattering by air, *J. Quant. Spectrosc. Ra.*, 95, 309–330, 2005.
- Vountas, M., Rozanov, V. V., and Burrows, J. P.: Ring effect: impact of rotational Raman scattering on radiative transfer in Earth's atmosphere, *J. Quant. Spectrosc. Ra.*, 60, 943–961, 1998.
- Wagner, T., Beirle, S., and Deutschmann, T.: Three-dimensional simulation of the Ring effect in observations of scattered sun light using Monte Carlo radiative transfer models, *Atmos. Meas. Tech.*, 2, 113–124, doi:10.5194/amt-2-113-2009, 2009a.
- Wagner, T., Deutschmann, T., and Platt, U.: Determination of aerosol properties from MAX-DOAS observations of the Ring effect, *Atmos. Meas. Tech.*, 2, 495–512, doi:10.5194/amt-2-495-2009, 2009b.
- Wagner, T., Beirle, S., Deutschmann, T., and Penning de Vries, M.: A sensitivity analysis of Ring effect to aerosol properties and comparison to satellite observations, *Atmos. Meas. Tech.*, 3, 1723–1751, doi:10.5194/amt-3-1723-2010, 2010.
- Webb, A. R., Bais, A. F., Blumthaler, M., Gobbi, G.-P., Kylling, A., Schmitt, R., Thiel, S., Barnaba, F., Danielsen, T., Junkermann, W., Kazantzidis, A., Kelly, P., Kift, R., Liberti, G. L., Misslbeck, M., Schallhart, B., Schreder, J., and Topaloglu, C.: Measuring Spectral Actinic Flux and Irradiance: Experimental Results from the Actinic Flux Determination from Measurements of Irradiance (ADMIRA) Project, *J. Atmos. Ocean. Technol.*, 19, 1049–1062, 2002.
- Woods, T. N., Prinz, D. K., Rottmann, G. J., London, J., Crane, P. C., Cebula, R. P., Hilsenrath, E., Brueckner, G. E., Andrews, M. D., White, O. R., VanHoosier, M. E., Floyd, L. E., Herring, L. C., Knapp, B. G., Pankratz, C. K., and Reiser, P. A.: Validation of the UARS solar ultraviolet irradiances: Comparison with the Atlas 1 and 2 measurements, *J. Geophys. Res.*, 101, 9541–9569, 1996.
- Young, A. T.: Rayleigh scattering, *Appl. Opt.*, 20, 533–535, 1981.